

Estimation of all-sky 1 km land surface temperature over the conterminous United States

Bing Li^a, Shunlin Liang^b, Xiaobang Liu^a, Han Ma^{a,*}, Yan Chen^a, Tianchen Liang^a, Tao He^a

^a School of Remote Sensing and Information Engineering, Wuhan University, Wuhan 430079, China

^b Department of Geographical Sciences, University of Maryland, College Park, MD 20742, USA

ARTICLE INFO

Guest editor: Jing M. Chen

Keywords:

Land surface temperature
All-sky
Random forest
MODIS

ABSTRACT

Land surface temperature (LST) is a crucial parameter for hydrology, climate monitoring, and ecological and environmental research. LST products from thermal infrared (TIR) satellite data have been widely used for that. However, TIR information cannot provide LST data under cloudy-sky conditions. All-sky LST can be estimated from microwave measurements, but their coarse spatial resolution, narrow swaths, and short temporal range make it impossible to generate a long-term, high-resolution, accurate global all-sky LST product. This study proposes a methodology for generating the all-sky LST product by combining multiple data from Moderate Resolution Imaging Spectroradiometer (MODIS), reanalysis, and ground in situ measurements using a random forest. Field measurements from the AmeriFlux and Surface Radiation Budget (SURFRAD) networks were used for model training and validation. Cloudy-sky and clear-sky LST models were developed separately. To further improve the accuracy of the cloudy-sky LST model, the conventional RF model was extended to incorporate temporal information. The models were validated using in situ LST measurements from 2010, 2011, and 2017 that were not used for the model training. For the cloudy-sky and clear-sky models, root-mean-square-error (RMSE) = 2.767 and 2.756 K, $R^2 = 0.943$ and 0.963 , and bias = -0.143 and -0.138 K, respectively. The same validation samples were used to validate both the MODIS LST product under clear-sky conditions and all-sky Global Land Data Assimilation System (GLDAS) LST product at 0.25° spatial resolution, with RMSE = 3.033 and 4.157 K, bias = -0.362 and -0.224 K, and $R^2 = 0.904$ and 0.955 , respectively. Additionally, the 10-fold cross-validation results using all the training datasets further indicate the model stability. The models were applied to generate the all-sky LST product from 2000 to 2015 over the conterminous United States (CONUS). Our product shows similar spatial patterns to the MODIS and GLDAS LST products, but it is more accurate. Both validation and product comparisons demonstrated the robustness of our proposed models in generating the all-sky LST product.

1. Introduction

Land surface temperature (LST) is the skin temperature of the uppermost layer of the earth's surface. It is a key parameter in land surface energy exchange and interactions between land and atmosphere. Therefore, it is a crucial study factor in many scientific fields such as climate change, energy balance, hydrology, agriculture, and ecology. Remote sensing data are used to obtain LST with high spatial and temporal resolution from regional to global scale (Li et al., 2013; Liang, 2005). In the past few decades, many LST products and algorithms based on infrared satellite data have been developed, such as from the Moderate Resolution Imaging Spectroradiometer (MODIS) (Ma et al., 2017;

Wan and Dozier, 1996) and Visible Infrared Imaging Radiometer (VIIRS) (Ma et al., 2018; Yu et al., 2005). However, due to the influence of clouds, LST values are valid only under clear-sky conditions. Research has shown that the data loss caused by cloud contamination exceeds 50%, and it is especially severe during the daytime (Crosson et al., 2012; Duan et al., 2017). Therefore, an appropriate method for LST estimation under all-sky conditions should be developed.

Several approaches have been proposed to address the missing values in LST products resulting from cloud contamination (Liang and Wang, 2019; Shen et al., 2015; Zhan et al., 2013). The algorithms used for this purpose can be divided into four classes: 1) temporal and spatial, 2) physically based, 3) passive microwave-data based, and 4) machine

* Corresponding author.

E-mail address: mahans@whu.edu.cn (H. Ma).

<https://doi.org/10.1016/j.rse.2021.112707>

Received 14 December 2020; Received in revised form 8 August 2021; Accepted 11 September 2021

Available online 24 September 2021

0034-4257/© 2021 Elsevier Inc. All rights reserved.

learning. Among them, temporal and spatial methods use spatiotemporal information of LST, considering its temporal variation law and spatial distribution characteristics. Spatial information-based methods establish the relationship between cloudy-sky pixels and the nearest clear-sky pixels mainly through interpolation, such as kriging, spline function and inverse distance weighting (Jackson et al., 2014; Neteler, 2010; Urquhart et al., 2013). However, the accuracy of these methods depends on the availability of nearby clear-sky pixels, which are limited in large areas of cloudy-sky pixels, leading to an unsatisfactory accuracy. Temporal information-based methods including interpolation or filtering, are to obtain the missing value from the time series of clear-sky LST (Pede and Mountrakis, 2018; Zeng et al., 2015). Moreover, MODIS LST has four observations from Terra and Aqua satellites, which provides the possibility to fill a gap using other clear-sky observations (Coops et al., 2007; Li et al., 2018). Some researchers combine spatial and temporal methods to gather more information for LST reconstruction (Metz et al., 2017; Zhang et al., 2018). Although the spatial and temporal methods use the variation of LST in time and space, they are based on clear-sky pixels, which results in a hypothetical clear-sky LST rather than the actual cloudy-sky LST (Zeng et al., 2018).

To estimate the real LST under cloudy-sky conditions, some methods combine physical processes data (Jin and Dickinson, 2000; Yu et al., 2014; Zeng et al., 2018; Zhang et al., 2015). A physical algorithm based on surface energy balance (SEB) was proposed by Jin and Dickinson (2000). The proposed method considered that the LST under cloudy-sky condition was affected by changing the solar radiation and downward longwave radiation. Thus, LST for a cloudy-sky pixel can be derived from a neighboring clear-pixel LST and the SEB difference between the two pixels. Then the method is improved by using both temporal and spatial information from neighboring clear-sky pixels to estimate the cloudy-sky LST for MODIS product (Yu et al., 2014). However, some physical parameters required in these methods, such as wind speed and air temperature, were difficult to obtain. Then, with the emergence of advanced remote sensing products, a two-step method was proposed by using multi-temporal LST and combined corresponding vegetation index to obtain a hypothetical LST and then correct the hypothetical LST based on SEB using solar shortwave irradiation data (Zeng et al., 2018). In addition, a scheme accounting for the solar-cloud-satellite geometry effect to estimate the LSTs of shadowed and illuminated pixels covered by clouds in the image has also been proposed (Wang et al., 2019). Moreover, a more generalized method that assimilates clear-sky LST into a surface energy balance equation has been recently proposed to estimate cloud-sky LST from MODIS and VIIRS data (Jia et al., 2021).

Passive microwave (PMW) remote sensing data provide another approach to estimate all-sky LST retrievals (Duan et al., 2017; Han et al., 2018; Zhou et al., 2015), and they are less affected by cloud contamination. However, there are also limitations in the LST retrieval from PMW measurements. For instance, PMW remote sensing data have a coarse spatial resolution of tens of kilometers, such as the Advance Microwave Scanning Radiometer-Earth Observing System (AMSR-E) with a 25 km resolution (Cavaliere et al., 2014). Moreover, PMW data have orbit gaps. In addition, the temperature obtained from PMW measurements is the subsurface temperature, in contrast with thermal infrared (TIR) LST that provides skin temperature (De Jeu, 2003; Prigent et al., 1999). The accuracy of the LST retrieval from passive microwave measurements is lower than that from TIR measurements by 3–5 K (Duan et al., 2017). Recently, some researchers have explored the possibility of combining PMW data and reanalysis data to estimate all-sky LST (Zhang et al., 2019c; Zhang et al., 2020). In contrast to PMW data, reanalyzed data is obtained by advanced land surface modeling and data assimilation techniques from satellite- and in situ observations. Reanalysis data involves the continuous monitoring without any gaps and can provide another possibility for all-sky LST retrieval (Long et al., 2020; Padhee and Dutta, 2020; Zhang et al., 2019c; Zhang et al., 2021).

Many LST estimation methods based on machine learning and deep learning have emerged (Wu et al., 2019; Zhang et al., 2020; Zhao and

Duan, 2020). Most of them construct a relationship between clear-sky MODIS LST and related variables and extend that relationship to all-sky conditions. However, the relationship constructed with clear-sky pixels may not apply to cloudy-sky conditions. Therefore, models that provide real cloudy-sky conditions LST using in situ LST measurements are relatively reliable. One type of in situ LST is the actual LST measured on the ground (Coll et al., 2005; Wan et al., 2002), which is difficult to obtain in a large area and limited to homogeneous and flat surfaces. Based on thermal radiative transfer theory, LST can also be calculated from the ground upwelling longwave radiation as well as emissivity and downwelling longwave radiation (Wang et al., 2008). Various longwave radiation measurement sites are available in the conterminous United States (CONUS), which produces sufficient representative in situ LST measurements for the training of machine learning models to produce all-sky LST estimates on a national scale.

This study aims to estimate all-sky LST over CONUS from both MODIS/Terra (MOD) and MODIS/Aqua (MYD) instantaneous clear-sky LST products and other information. We choose the random forest (RF) algorithm to build a non-linear relationship between LST and related variables, and we developed a temporal RF (T-RF) algorithm for a cloudy-sky model, which considers the temporal variation information of LST. To accurately estimate cloudy-sky LST, we incorporated several all-sky surface radiation variables and reanalysis data. The surface radiation variables help capture the physical process of surface heat exchange. To enhance the model performance, we constructed separate models for clear-sky conditions and cloudy-sky conditions and compared the models based on two algorithms for cloudy-sky conditions.

The remainder of this paper is organized as follows. Section 2 introduces the data sources. Section 3 describes the algorithms and the process chain in detail. Section 4 presents the results of model performance and compares it with other products. Section 5 discusses the advantages and limitations of this study. Section 6 presents the conclusions.

2. Data

The data used in this study include 1) in situ LST measurements for model training and validation, 2) reanalysis dataset used for the model as well as comparison, and 3) remotely sensed data as model inputs (i.e., surface variables, radiation variables, and geolocation information). Table 1 summarizes the products used in this study. Each type of data (i.e., in situ measurements, remotely sensed data, and Global Land Data Assimilation System (GLDAS) data), as well as the pre-processing steps, are described in detail in the following sections.

Table 1
Summary of remotely sensed data used in this study.

Variables	Product	Resolution (spatial/temporal)
Land surface temperature (LST)	MOD11L2, MYD11L2	1 km/ instantaneous
View angle, solar angle, and height	MOD03, MYD03	1 km/ instantaneous
Snow cover	MOD10A1, MYD11A1	500 m/daily
Land cover (LAC)	MCD12Q1	500 m
Broadband Emissivity (BBE)	GLASS03A01	1 km/8 d
Downward longwave radiation (LWDN)	GLASS06M01	1 km/ instantaneous
Downward Shortwave Radiation (DSR)	GLASS05B01	0.05°/daily
Surface Broadband Albedo (Albedo)	GLASS02A06	1 km/8 d
Leaf area index (LAI)	GLASS01A01	1 km/8 d

2.1. In situ measurements

To obtain the in situ LST for model training and validation, in situ longwave radiation measurements were collected at two observation networks, namely AmeriFlux and Surface Radiation Budget (SURFRAD). The AmeriFlux network, supported and maintained by the Lawrence Berkeley National Laboratory, was established to connect research on field sites representing major climate and ecological biomes, and it has 110 current active sites (Baldocchi et al., 2001). Some sites from the AmeriFlux network have longwave radiation records. SURFRAD networks support climate research with accurate, continuous, long-term measurements of the surface radiation budget over the United States (Augustine et al., 2000; Augustine et al., 2005). Currently, seven SURFRAD stations are operating in climatologically diverse regions. To reduce the uncertainties, strict quality control should be conducted on all the sites. First of all, we checked the temporal continuity and removed the individual sites with few and continuity records. Then, one set of site data was kept from the available nearby sites to avoid the duplication and interference. Finally, we selected all sites with longwave radiation measurements on CONUS from 2003 to 2017, thus including 89 sites from AmeriFlux and 7 sites from SURFRAD. In order to verify the representativeness of the sites, we extracted the 30 m LST data of Landsat8 from 2016 to 2018 on the Google earth engine (Ermida et al., 2020). The extracted pixels were within 1 km around the sites, and the standard deviation (STD) value in the extracted window was calculated to represent the heterogeneity. The histogram statistic of multi-year average STD for each site is shown in Fig. 1 (b). The result shows that selected sites are highly representative, and the STD of all sites is less than 3 K. Since the observation time of Landsat is during the daytime in the morning, the heterogeneity at nighttime is lower (Duan et al., 2019; Wang and Liang, 2009). However, the Aqua overpasses in afternoon, which probably increases the heterogeneity (Li et al., 2014). Fig. 1(a) shows the spatial distribution and STD of the 96 in situ observation sites used in this study.

The ground-based LST at the in situ observation sites was retrieved from the surface upwelling and atmospheric downwelling longwave radiation using the Stefan–Boltzmann law:

$$T_s = \left(\frac{F_{up} - (1 - \epsilon)F_{dn}}{\sigma \epsilon} \right)^{\frac{1}{4}}, \quad (1)$$

where T_s is the LST, F_{up} is the longwave upwelling radiation, F_{dn} is the longwave downward fluxes, σ is the land surface of broad-band emissivity, and ϵ is the Stefan–Boltzmann's constant ($5.67 \times 10^{-8} \text{ Wm}^{-2} \text{ K}^{-4}$). The surface broadband emissivity of the flux towers was obtained from the broad band emissivity (BBE) product referred to in Sect. 2.2.

2.2. Remotely sensed data

The remotely sensed data used in this study are summarized in Table 1. The MODIS LST products (i.e., MOD11L2 and MYD11L2) in Collection 6, are at a 1 km spatial resolution. They can provide instantaneous LSTs in daytime and nighttime from different satellite viewing times, retrieved by the generalized split-window (GSW) method (Wan and Li, 1997). Pixels with quality control (QC) flags of clouds were identified as cloudy pixels, and clear-sky LST was used for modeling and comparison. The MOD03 and MYD03 products with 1 km resolution represent the geolocation products, and they provide the solar zenith angle (SZA), solar azimuth angle (SAA), viewing zenith angle (VZA), viewing azimuth angle (VAA), and surface elevation variables. The relative azimuth angle was calculated from SAA and VAA. The geolocation products were also utilized to match pairs between in situ longwave radiation measurements and satellite LST. Furthermore, the MODIS land cover product (MCD12Q1) provides land cover types once a year with a 500 m resolution. The daily MODIS snow cover data (MOD10A1 and MYD11A1) in Collection 5 was utilized to identify snowy conditions at a 500 m resolution. They were not upscaled to 1 km to better represent the surface condition of the site.

Five products from the Global LAnd Surface Satellite (GLASS) suite were used (Liang et al., 2020), including BBE, surface longwave net radiation (LWNR), downward shortwave radiation (DSR), surface broadband albedo (albedo), and leaf area index (LAI). The BBE product (GLASS03A01) was derived from Advanced Very High Resolution Radiometer (AVHRR) and MODIS optical data using newly developed algorithms (Cheng et al., 2016; Cheng et al., 2014). BBE was used to calculate the in situ LST. For the GLASS LWNR (GLASS06M01), a new parameterized scheme was proposed to calculate instantaneous downward longwave radiation (LWDN) based on MODIS data (Cheng et al., 2017; Yang and Cheng, 2020). As for the LWDN under cloudy-sky condition, Yang and Cheng (2020) discussed the algorithm for estimating LWDN from the derived active and passive cloud property parameters, such as cloud thickness, cloud-base temperature. For that, the LWDN variable in the LWNR product was used. The DSR product (GLASS05B01) provided daily DSR values produced using MODIS data based on a look-up table from radiative transfer models established with and without clouds (Zhang et al., 2019b). The GLASS albedo was produced using MODIS and AVHRR data from a direct-estimation algorithm (Liu et al., 2013; Qu et al., 2014). The GLASS LAI product was produced using the MOD09A1 product by the general regression neural network method (Xiao et al., 2014; Xiao et al., 2016). The GLASS products mentioned above have the same spatial resolution of 1 km, except for DSR with 0.05°.

The temporal resolution of these products is eight days (use 8 d to represent the eight days in the following), except for DSR (daily) and the

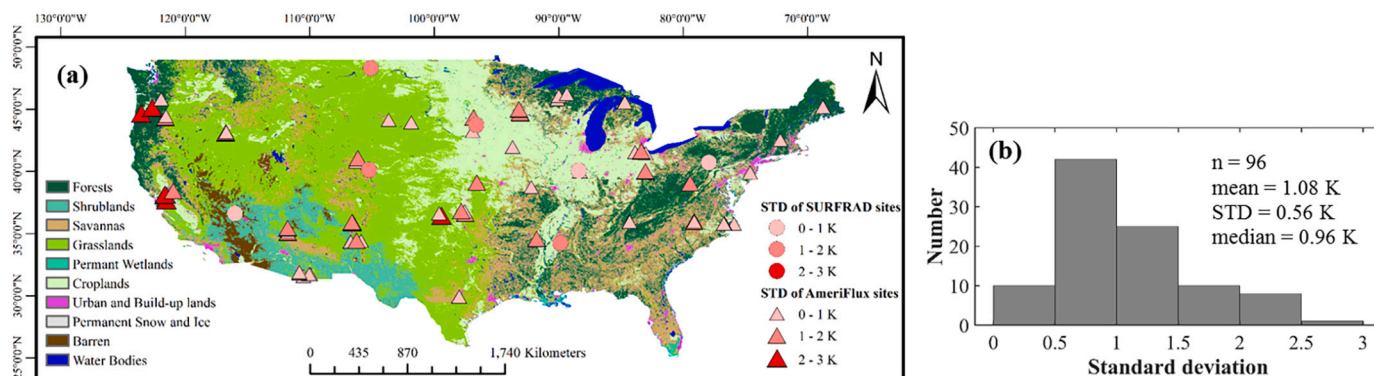


Fig. 1. (a) Spatial distribution of selected sites in the study area. SURFRAD network is shown with circles while AmeriFlux network is shown with triangles. The STD value of each site is represented by different colors. Land use cover types for 2011 (background colored shading) are from a MODIS land use cover product at a 500 m spatial resolution. (b) The histogram of multi-year average values of standard deviation for each site is shown.

LWDN (instantaneous). All of them are global land surface products for all-sky conditions. To obtain daily values of each 8 d variable (i.e., BBE, Albedo, LAI), interpolation methods were utilized for each product. As for BBE and Albedo, the nearest neighbour interpolation method was used, as these two variables are nearly invariant within eight days. However, there may be snowy days leading to a mutation. Therefore, we identified the BBE value of snowy days as 0.985 according to the snow cover product. The BBE data with good quality (QC = 0) was used. As for LAI, the linear interpolation method was used to obtain daily LAI, which would represent the trend of LAI.

The rationale for choosing the variables in these products are given in Sect. 3.

2.3. GLDAS LST data

The GLDAS data represent global reanalysis data containing a series of land surface states and flux. It incorporates both ground- and space-based observation systems to constrain the modeled land surface states and flux (Rodell et al., 2004). There are four different models, namely MOSAIC, NOAH, CLM, and VIC, to simulate the hydrological fields of GLDAS for different products. In this study, the instantaneous LST was used in the GLDAS NOAH dataset with 0.25° spatial resolution at a 3-h time scale. GLDAS LST was temporally interpolated to the value at the MODIS observation time via a cubic spline interpolation and resampled to 1 km using the nearest neighbour method.

3. Methods

The overall framework of the process developed in this study is shown in Fig. 2. First, parts of the samples were compiled for model training and validation, and the remaining samples were used as an independent dataset for the model evaluation. Subsequently, the mean decrease impurity (MDI) method was used to remove the redundant variables. After the variables were determined, grid research was

combined with random search to determine the parameters of the final model. The RF and T-RF are described in Sect. 3.2.

3.1. Temporal RF model

RF is a machine learning method proposed by Breiman (2001) and has been widely used for regression and classification (Belgiu and Drăguț, 2016; Gibson et al., 2020; Kuter, 2021; Pelletier et al., 2016). In regression tasks, the RF method is outstanding in constructing complex nonlinear relationships between predictor and response variables for a large dataset (Hutengs and Vohland, 2016). The RF method has the characteristics of randomness in the selection of samples and attributes. This counterintuitive strategy leads to better performance compared to several other machine learning methods and is robust against overfitting (Liaw and Wiener, 2002).

RF is an ensemble algorithm that consists of multiple decision trees (Breiman, 2001). In a random forest, each decision tree grows on a bootstrap sample of the training data. A decision tree is a tree-like model with multiple nodes. The dataset is segmented at each node using a random subset of predictors through information gain, Gini index or other methods to construct the splitting rules. Besides, the number of predictors is limited for a split, which can reduce the computational complexity of the algorithm and the correlation among the trees. The split process of RF introduces randomness that contributes to a less variable and more reliable result (Hutengs and Vohland, 2016). Generally, the split process is repeated recursively on each subset until the node contains similar samples, or the splitting no longer improve the predictions. The final result is obtained from all decision trees by voting (in case of classification) or averaging (in case of regression) (Pelletier et al., 2016). In this study, model training and predictions were undertaken using the scikit-learn package in Python (Pedregosa et al., 2011).

RF method is widely used in remote sensing (Belgiu and Drăguț, 2016). However, it is common to input several independent variables and not consider temporal information. Recent studies have combined

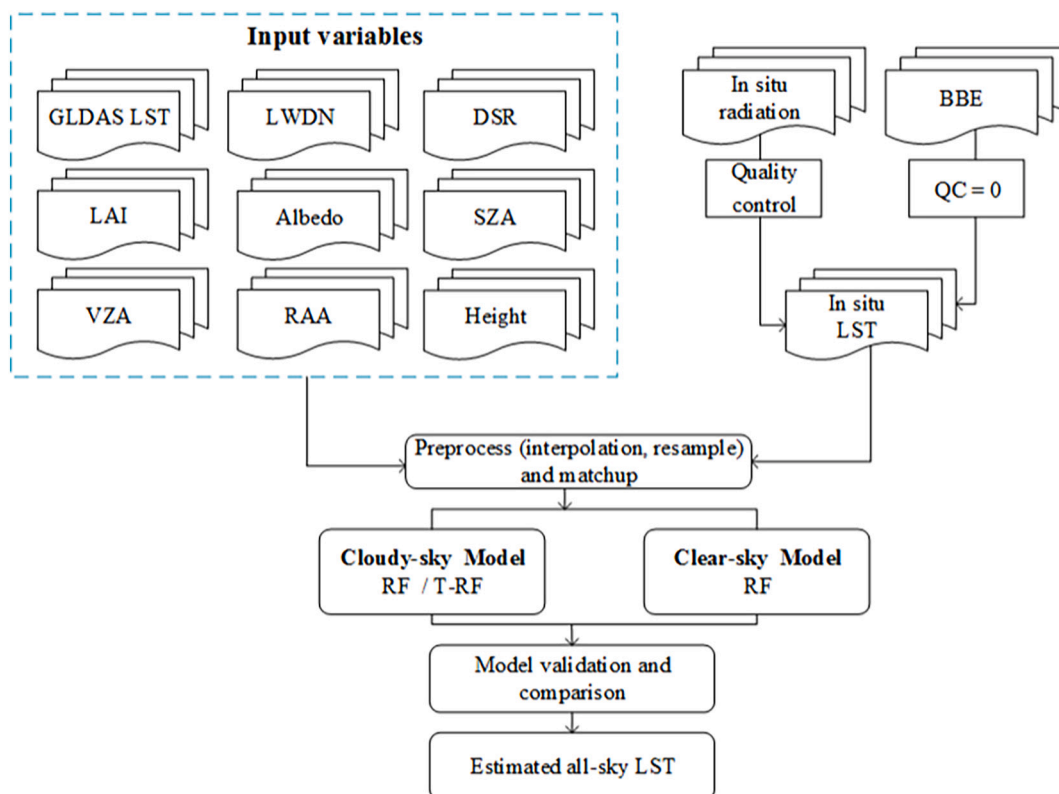


Fig. 2. Flowchart of the process to estimate all-sky LST from MODIS data.

spatiotemporal information with RF in other fields (Wei et al., 2019; Wei et al., 2020). As LST varies considerably over time, many studies have utilized temporal information to reconstruct or estimate LST under cloudy-sky conditions (Kilibarda et al., 2014). We combined the time-weighted LST information with the RF model, thus creating the T-RF model to estimate cloudy-sky LST. Therefore, the T-RF model considers not only the information of multiple variables but also the LST in the time dimension. The temporal characteristic P_t in each pixel can be expressed as

$$P_t = \frac{\sum_{l=1}^L \frac{1}{dt_l^2} P_l}{\sum_{l=1}^L \frac{1}{dt_l^2}} \quad (2)$$

In the equation, dt_l represents the temporal distance, and L represents the prior or later l days for the same pixel, P_l represents the LST on l day. Considering the variation of LST, the available observations at almost the same time within 8 days were used.

3.2. Model training

All clear-sky and cloudy-sky samples from 2003 to 2009 and 2012–2016 were compiled. Usually, in RF algorithm, approximately two-thirds of the samples are used for model training and the remaining are for model validation (Breiman, 2001). The other samples from the other three years (2010, 2011, and 2017) were used as independent datasets for validation.

We initially selected the following variables: DSR, LWDN, LAI, SZA, VZA, RAA, surface elevation (Height), GLDAS LST (GLST) and broadband albedo that contains black-sky albedo and white-sky albedo in the three bands of shortwave (B-SH, W-SH), visible (B-VIS, W-VIS), and near infrared (B-NIR, W-NIR). LST was determined by the difference between incident and outgoing energy in the process of surface energy exchange. According to Eq. (1), longwave radiation is essential in this process. Meanwhile, DSR can reflect the significant changes in solar radiation caused by clouds that influence LST to a certain extent. Thus, LWDN and DSR were used to reflect the contributions of long and shortwave radiation to LST. In addition, the LAI and broadband albedo were used to represent surface conditions such as vegetation coverage, soil moisture, and land cover type, which also influence LST. In addition, the prediction of LST at a finer resolution is influenced by geographical and topographical parameters including surface elevation, and the view and relative angle of the satellite and the sun (Zhao et al., 2019). All abovementioned variables were at high resolution for all-sky conditions. Moreover, the reanalysis data were available in all-sky conditions but with coarse resolution. The LST of the GLDAS was also utilized as an input variable.

To prevent the model from being too complex thus leading to overfitting, the model was further adjusted by selecting the most important variables and adjusting the parameters. The mean decrease in impurity (MDI) was widely used in tree models as a variable importance measure because of its high efficiency and stability (Han et al., 2016; Louppe et al., 2013). The MDI index shows the total decrease in node impurities from splitting on the variable, averaged over all trees; and it reflects the contribution of the parameters to the model. In this study, we used the MDI method to filter the variables. MDI was used separately for the clear-sky and cloudy-sky condition samples, and some variables with low contributions were removed. The MDI results of the cloudy-sky and clear-sky models are shown in Fig. 3. The results indicate that GLST, temporal characteristic P , and radiation data are the main contributors to the models. However, the variables with low MDI values did not indicate an insufficient correlation with LST. This may have been caused by a higher correlation with the variables at the ranking top, which is also a characteristic of the MDI method. We eliminated the variables with an MDI value of less than 1%. The variables ranked in the last four were eliminated. There were no obvious changes in the model accuracy after feature selection, which demonstrates that the eliminated variables

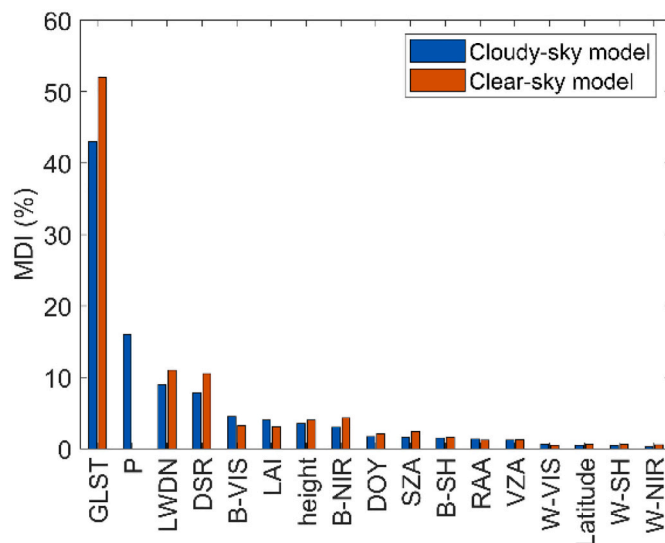


Fig. 3. MDI results of cloudy-sky and clear-sky models.

were redundant for the model construction. After feature selection, the LST estimation can be expressed as: $LST = f(\text{GLST}, P, \text{LWDN}, \text{DSR}, \text{B-VIS}, \text{LAI}, \text{height}, \text{B-NIR}, \text{DOY}, \text{SZA}, \text{B-SH}, \text{RAA}, \text{and VZA})$. The temporal characteristic P was only used in the cloudy-sky model.

Several important RF parameters also required adjustments. Accordingly, n estimators, max depth, max feature, and min sample leaf of the RF model were adjusted after the feature selection. N estimator is the RF frame parameter that determines the maximum number of trees. Max depth, max feature, and min sample leaf limit the maximum number of the depth and features in the tree structure, and the minimum number of samples required to split an internal node, respectively (Pelletier et al., 2016). We used grid search combined with a random search to determine the parameters. The grid search performs multiple cross-validations for each parameter combination within a certain range according to the accuracy of the model, and it selects the parameter combination with the highest average score as the best parameter. This method can provide accurate parameter optimization results, but the efficiency is significantly low for large datasets. Therefore, we firstly used random search to obtain a set of parameters, which were used as a reference for the setting of grid search, and then obtained the optimal parameters through the grid search. After tuning, the model parameters were set as follows: n estimators = 420, max depth = 43, max feature = 9, min samples leaf = 1.

3.3. Evaluation approaches

Both independent validation with samples from three years (2010, 2011, and 2017) and 10-fold cross-validation (CV) were used for the model validation. In the process of 10-fold CV, the training dataset was divided into ten folds. Among them, nine folds were utilized to train the model, and one was used for model validation. This process was repeated 10 times until all 10 folds were used for the independent validation. The above validation methods were also used to examine the sensitivity of the models. In addition, we evaluated the model performance on individual sites, seasons, and land cover types. Lastly, we applied the final models to the CONUS for 2000 to 2015. The generated LST product was compared with the corresponding MODIS LST and GLDAS LST.

4. Results analysis

4.1. Model training and validation

Fig. 4 shows the density scatterplots of the training results using data from 2003 to 2009 and 2012–2016. For the cloudy-sky and clear-sky models, the root-mean-square-error (RMSE) = 2.536 and 2.354 K, $R^2 = 0.952$ and 0.973 , bias = -0.005 and 0.005 K, respectively. The training results indicate that both models performed well. The clear-sky model presented a slightly better accuracy than the cloudy one in the model training. The validation results using data from 2010, 2011, and 2017 are shown in Fig. 5. The two models have comparable accuracy, with RMSE = 2.767 and 2.756 K, $R^2 = 0.943$ and 0.963 , and bias = -0.143 and -0.138 K, respectively. The training and individual validation results suggest that both fitting models had no obvious overfitting and can robustly estimate LST. The 10-fold CV results, shown in Fig. 6, can further verify the stability of the model performance. According to the training and 10-fold CV results, the clear-sky model presents slightly higher accuracy, which is comparable to the validation results. Therefore, the obtained difference was probably caused by the different datasets used. In general, ancillary products present larger uncertainty under cloudy-sky conditions. The proposed T-RF method for the cloudy-sky model effectively provided an accuracy comparable with the clear-sky model. Overall, the accuracy of the model indicates the feasibility of the proposed methods for estimating all-sky LST.

As shown in Table 2, we further derived the statistics from the individual validation datasets for the different overpass-time observations and different satellites for the cloudy-sky and clear-sky models separately. The results indicate that the accuracy of nighttime is higher than daytime in both models. In the daytime, the in situ LST measurements may suffer from the influence of solar radiation, which brings uncertainty. During the daytime, the spatial thermal heterogeneity of the land surface is relatively higher, and the TIR directional anisotropy is higher and more complicated (Cao et al., 2019; Lagouarde et al., 2012; Xu et al., 2019). In addition, the LST value during daytime is relatively higher than at nighttime, which can result in a higher RMSE value. The higher accuracy at nighttime than at daytime has also occurred in the validation of other LST products (Duan et al., 2018; Shwetha and Kumar, 2016; Wang and Liang, 2009). For the cloudy-sky model, the accuracy of MOD is higher than that of MYD, with respective RMSE values of 2.71 and 2.82 K. For the clear-sky model, the RMSE is similar, but the bias of MYD is -0.27 K, which is larger than that of the MOD (0.01 K). Both models show the relatively higher accuracy of MOD. This probably occurs due to the earlier observation time of MOD at which the spatial thermal

heterogeneity of the land surface is generally lower than that in the afternoon when MYD overpasses.

In generating of the product, we established two models using the T-RF or RF method for the cloudy-sky models. The same cloudy-sky datasets were used for comparison. The training and validation results for the T-RF and RF methods are shown in Table 3. The results show that the T-RF algorithm performs slightly better than the traditional RF in terms of both the training and validation results. The error histograms of the models and MODIS LST against in situ LSTs using independent validation datasets are shown in Fig. 7. The error distribution of the T-RF cloudy-sky model (Fig. 7a) performed slightly better than that of the RF-based cloudy-sky model (Fig. 7b) with mean values of -0.14 and -0.19 K and STD values of 2.76 and 2.90 K, respectively. Although the accuracy between the two models is less than 0.2 K, it is the average error of all stations. The results obtained from the clear-sky model (Fig. 7c) outperformed MODIS LST (Fig. 7d), with mean values of -0.14 and -0.36 K, and STD values of 2.75 and 3.01 K, respectively.

4.2. Model performance at individual sites

Fig. 8 shows the spatial distributions and histograms of the RMSE calculated by individual validation results of the cloudy-sky model, clear-sky model, and corresponding MODIS clear-sky LST. The background colour represents the elevation data from GMTED2010. For the cloudy-sky model (Fig. 8a), the RMSE values of all individual sites ranged from 1.67 to 3.89 K. According to the corresponding histograms, over 70% of the stations have RMSE values smaller than 3 K. However, it has a relatively lower accuracy on the complicated terrain in the western part of the CONUS. In regions with relatively high elevations, complex atmospheric conditions affect the estimation of surface parameters. In addition, complex topography increases TIR directional anisotropy (Cao et al., 2021; Jiao et al., 2019), leading to more uncertainty in estimating LST. This phenomenon also exists in MODIS LST products (Fig. 8e) and other research (Zhao et al., 2020). For the clear-sky models, the results of RMSE values and MODIS LST were 1.62–4.32 K and 1.66–4.88 K, respectively. The accuracy of the clear-sky and cloudy-sky models are comparable, and the RMSE values of over 60% of the sites are below 3 K. Nevertheless, the RMSE value of a few sites exceeds 4 K. The relatively higher RMSE may be caused by a higher LST value under clear-sky conditions. In contrast to cloudy-sky model, temporal information is not used in the clear-sky model. Moreover, few sites with large errors appear in the center of the CONUS only in the clear-sky model. These errors likely occurred because parts of the in situ measurements were affected by the solar radiation under clear-sky conditions. Solar

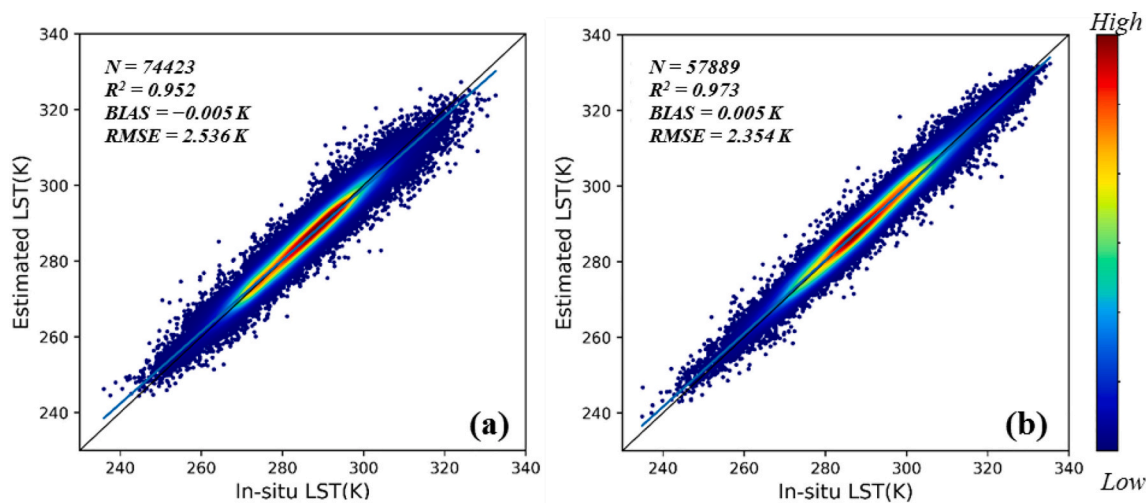


Fig. 4. Density scatterplots of model training for (a) cloudy-sky and (b) clear-sky models.

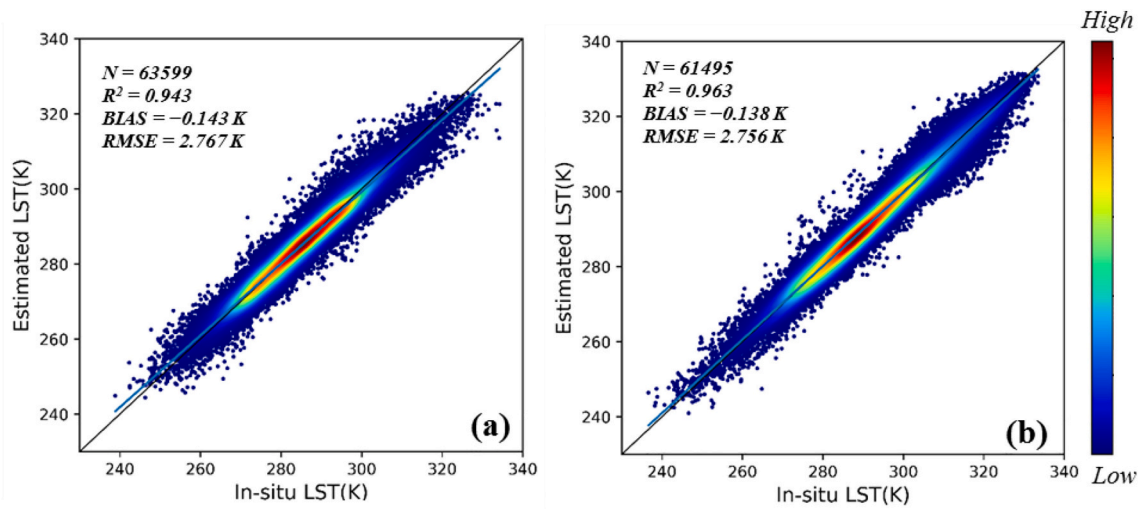


Fig. 5. Density scatterplots of model validation for (a) cloudy-sky and (b) clear-sky models.

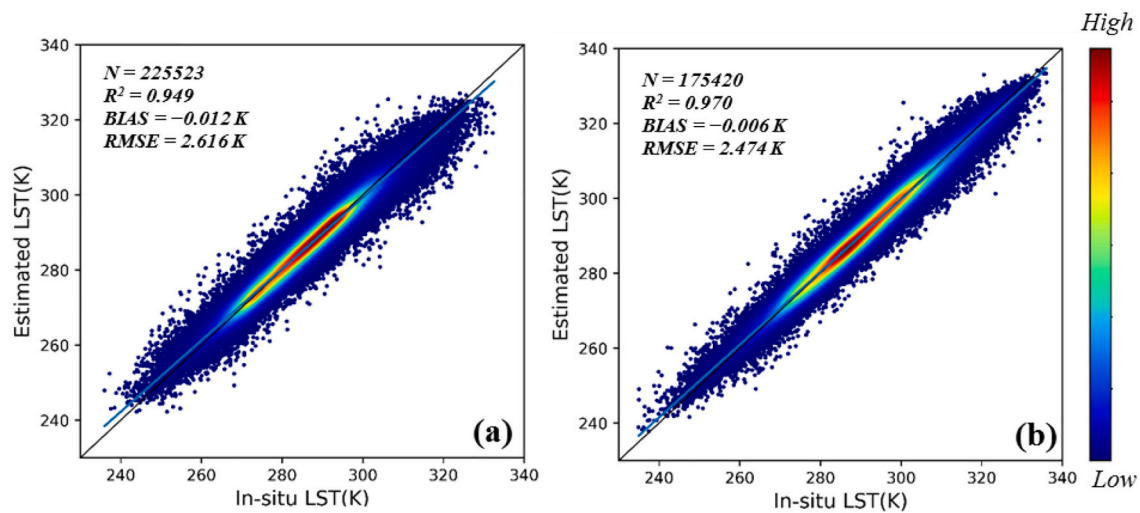


Fig. 6. Density scatterplots of sample-based cross-validation results for (a) cloudy-sky and (b) clear-sky models.

Table 2
Individual validation of the models at daytime and nighttime, and of MOD and MYD.

		R ²	RMSE (K)	Bias (K)	N
Cloudy	Daytime	0.94	3.09	0.15	32,025
	Nighttime	0.94	2.40	-0.44	31,574
Clear	Daytime	0.94	3.02	0.13	32,793
	Nighttime	0.92	2.41	-0.44	28,702
Cloudy	MOD	0.94	2.71	-0.13	30,724
	MYD	0.94	2.82	-0.15	32,875
Clear	MOD	0.96	2.76	0.01	28,778
	MYD	0.96	2.75	-0.27	32,717

Table 3
Training and validation results of T-RF and RF methods for the cloudy-sky model.

	Training			Validation		
	RMSE (K)	Bias (K)	R ²	RMSE (K)	Bias (K)	R ²
T-RF	2.536	-0.005	0.952	2.767	-0.143	0.943
RF	2.621	0.006	0.949	2.914	-0.191	0.937

radiation also increases the LST heterogeneity and TIR directional anisotropy, resulting in differences between in situ and MODIS pixel-scale LST (Cao et al., 2019; Wang and Liang, 2009). Overall, the accuracy of individual sites of the cloudy-sky model and clear-sky models were generally similar, and the accuracy of the clear-sky model was comparable to MODIS LST.

4.3. Model performance in seasons and land cover types

Fig. 9 shows the validation statistics of the proposed models for each season. The RMSE results (Fig. 9a) show the comparable accuracy of the cloudy-sky and clear-sky models, and both models show relatively higher uncertainty in spring and summer. The reason for that may be that these seasons represent the growing and peak seasons of vegetation, which can affect the LST values. The R² values (Fig. 9b) of the cloudy-sky model are lower in spring and summer, and the R² values of the clear-sky model are all higher than those of the cloudy-sky model. The absolute bias values in summer and winter are relatively higher (Fig. 9c). However, the biases in all seasons are not large, and the maximum absolute value is below 0.3 K. In general, seasonal differences in the accuracy of the models exist, but they are not significant.

Table 4 lists the validation results of the cloudy-sky and clear-sky

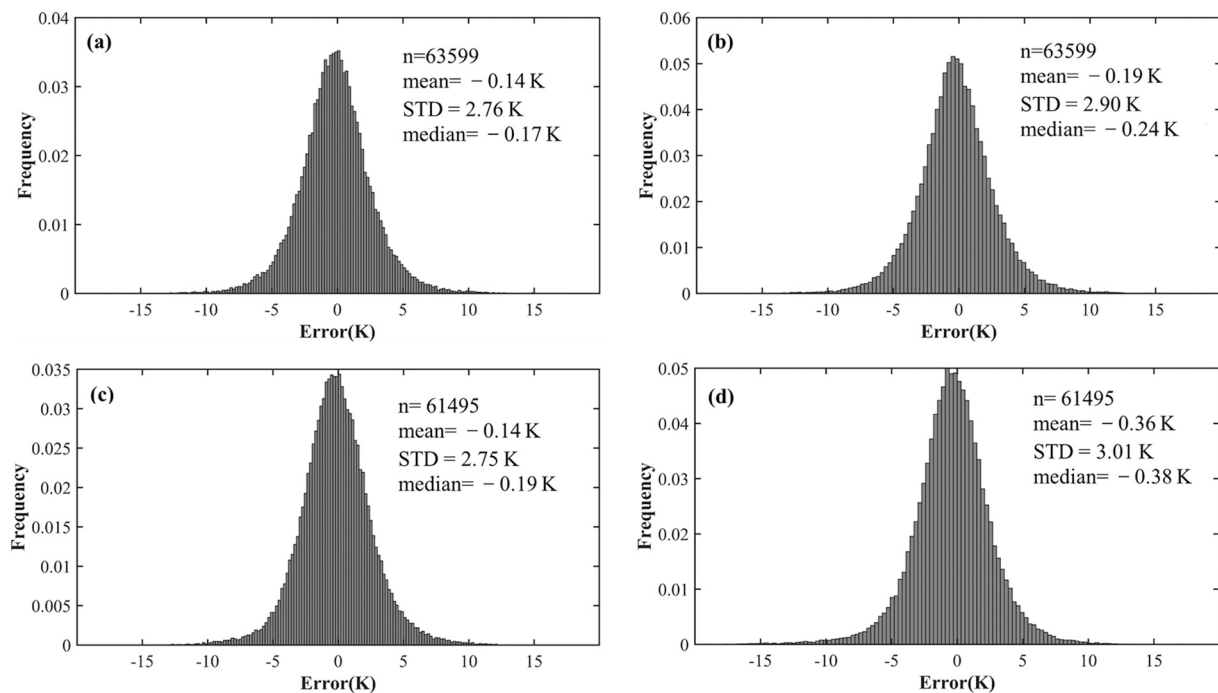


Fig. 7. Error histograms of (a) T-RF cloudy-sky model, (b) RF cloudy-sky model, (c) clear-sky model, and (d) MODIS clear-sky LST against independent in situ LSTs.

models for different land cover types. Among all land cover types, forest presented the highest accuracy, and the RMSE values in both models were less than 2.5 K. The accuracies of shrublands and grasslands were slightly lower than those of other vegetation types. Except for barren and snow/ice, the other land cover types presented similar validation results. The reason for the relatively poor performance of barren and snow/ice may be the high albedo and low specific heat capacity in these areas. For the barren land, there are significant biases with -0.56 K and -0.26 K under the cloudy-sky and clear-sky models, respectively. The LST may be underestimated due to the overestimation of emissivity on barren land (Duan et al., 2019; Zhang et al., 2019a). Otherwise, there is a limited amount of available snowy observations in CONUS, affecting the model stability under snowy conditions. The poor accuracy of the LST on snow/ice and barren surface is also reflected in other studies (Williamson et al., 2017; Zhang et al., 2019a; Zhang et al., 2021). In general, there were no significant differences between the results for different land cover types. In the proposed models, the differences between the maximum and minimum RMSE values were less than 2 K, which is consistent with the results obtained in other studies (Yoo et al., 2020).

4.4. Spatial pattern and temporal variability analysis

The proposed T-RF model was used for cloudy-sky pixels. However, for a small part of the pixels, there were no available clear-sky pixels. According to the rough statistics of the training and validation datasets, less than 5% of them did not have a match for clear-sky LST. Therefore, the traditional RF method was supplemented with T-RF for a small number of cloudy-sky pixels. Sect. 5 Fig. 10 shows the MOD daytime LST images (a–d), corresponding estimated all-sky LST images (e–h), and GLDAS LST images (i–l) at 93, 180, 276, and 360 Julian days in 2010. It is clear that the original MODIS LSTs show different extents of missing areas caused by cloud contamination, whereas the estimated LSTs present spatially continuous results. For the same day, the three products show a similar spatial pattern on clear-sky conditions. The spatial distribution follows a latitudinal gradient with relatively lower values in higher latitude areas caused by the change in solar radiation. In the summer and autumn, the eastern area has relatively higher LST values

than the western area due to the forest and cropland in the eastern area, which mitigates the effects of solar heating (Li et al., 2018). In addition, all of them show the same seasonal LST dynamics.

Despite the observed similarities, there are differences among the datasets. Although the GLDAS LST can demonstrate the overall spatial pattern of LST, it is inferior compared to the other two products in spatial details, especially in areas with complicated terrain (e.g., western part of CONUS). The density scatterplots of the GLDAS LST, clear-sky MODIS LST, Stefan-Boltzmann derived LST, and estimated LST using the validation dataset are shown in Fig. 11. The accuracy of the clear-sky MODIS LST (Fig. 11b) is RMSE = 3.033 K, Bias = -0.362 K, $R^2 = 0.955$, which is comparable but relatively lower than that of the clear-sky model (Fig. 6b). The uncertainty of the estimated all-sky LST was better (RMSE of 2.870 K) than that of the GLDAS LST (4.157 K). The R^2 value also improved from 0.904 (GLDAS LST) to 0.954 (estimated LST). The proposed model effectively improved the dispersion of GLDAS LST in the low- and high-temperature regions at both ends, which demonstrates the improvement of the estimated all-sky LST obtained in this study. Although previous studies had already considered common ancillary data such as NDVI and DEM (Hutengs and Vohland, 2016), our research introduces DSR, albedo, LAI, and other types of data. The LWDN variable was used for the first time, and it provides a greater contribution to the LST estimation compared to other inputs. The Stefan-Boltzmann derived LST (Fig. 11c) was retrieved from LWDN and surface upwelling longwave radiation from LWNRR product and BBE using the Stefan-Boltzmann law. The accuracy of the Stefan-Boltzmann derived LST is RMSE = 4.128 K, which is comparable to GLDAS LST, but lower than the estimated LST. The proposed algorithm can accurately obtain the all-sky LST and broadly represent the original thermal pattern of the study area. Furthermore, the LSTs of both large cloud-covered regions and regions covered by small clouds were effectively estimated, thus representing an advantage over traditional methods.

Fig. 12 shows a temporal comparison among the estimated LST, in situ LST, and MODIS LST over six sites from different regions in 2010. The observation time of the data is the same as that of the daytime MOD LST. The black and red lines represent the in situ LST and estimated all-sky LST, respectively. The corresponding MODIS LST under clear-sky conditions is shown as a blue circle. The temporal variability of the six

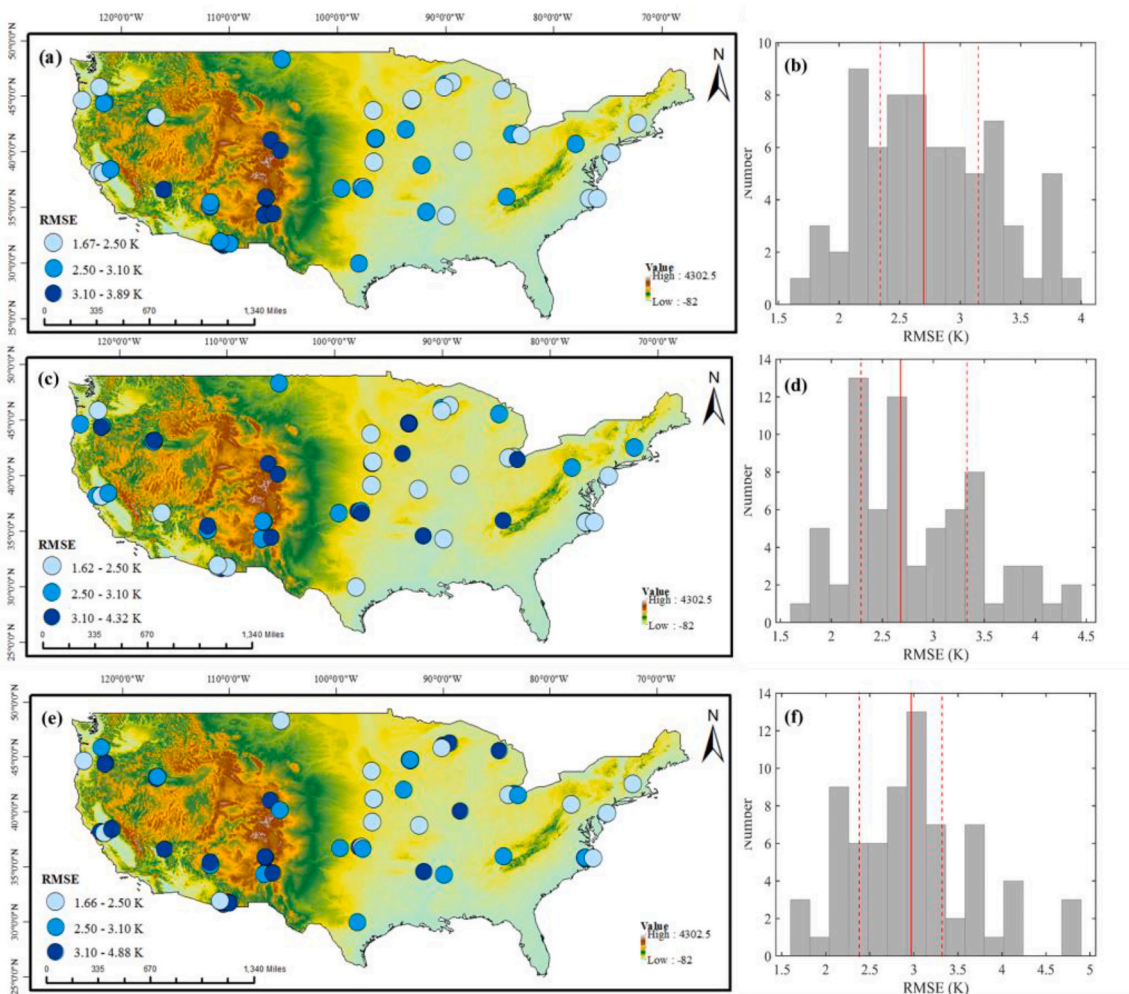


Fig. 8. RMSE spatial distributions (left) and histograms (right) of (a, b) cloudy-sky model, (c,d) clear-sky model, and (e, f) MODIS clear-sky LST. The spatial distribution figures are based on the DEM background. The red lines in the histograms represent 25%, 50%, and 75% of the sites. (For interpretation of the references to colour in this figure legend, the reader is referred to the web version of this article.)

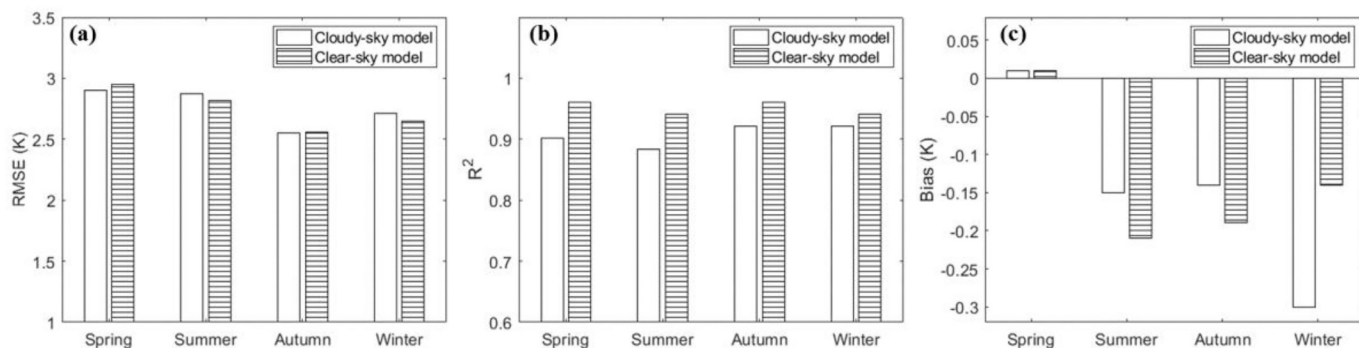


Fig. 9. (a) RMSE, (b) R^2 , and (c) bias values of the validation results of the proposed models during spring, summer, autumn, and winter.

sites indicates that the estimated LST sufficiently captured seasonal and daily changes, with an accuracy comparable to the MODIS LST. It should be noted that there were days when high LSTs sharply dropped, and the estimated LST can capture such low values, as shown in Fig. 11.a (DOY 330). Because the variables used are instantaneous or daily, the proposed method performs better than traditional methods, such as temporal interpolation, for capturing extreme and sudden weather conditions (Metz et al., 2014). In addition, all estimated LST time series presented excellent temporal consistency with the in situ LSTs at

different sites, at RMSE <3.27 K, bias <1.24 K, and $R^2 > 0.96$.

5. Discussion

In this study, all-sky LST was estimated using the T-RF and RF models by constructing a non-linear relationship between the reanalysis data, radiation variables, land surface characteristic variables, and in situ LSTs. The accuracy of the estimated all-sky LST is acceptable. There was no significant difference between the validation results of the clear-sky

Table 4
Validation results of cloudy-sky and clear-sky models for different land cover types.

Land cover types	Cloudy-sky model			Clear-sky model		
	RMSE (K)	Bias (K)	R ²	RMSE (K)	Bias (K)	R ²
Forest	2.27	-0.08	0.94	2.29	-0.18	0.96
Shrubland	3.35	-0.14	0.94	2.58	0.04	0.98
Savannas	2.91	-0.07	0.94	2.59	0.07	0.94
Grassland	3.15	-0.27	0.94	2.80	-0.27	0.96
Wetlands	2.51	-0.15	0.92	2.25	-0.25	0.98
Croplands	2.57	-0.09	0.96	2.99	-0.19	0.96
Urban	2.83	-0.54	0.94	3.39	-0.18	0.94
Barren	3.24	-0.56	0.92	3.71	-0.26	0.85
Snow/ice	3.46	0.14	0.83	3.87	0.88	0.85

(RMSE = 2.756 K) and cloudy-sky (RMSE = 2.767 K) models, and the clear-sky estimations are comparable to the corresponding MODIS LST products on a temporal and spatial scale, showing high consistency. In addition, there were no obvious differences in the accuracy of the models for Terra and Aqua MODIS observations during the daytime or nighttime, which demonstrates the stability of the model at different observation times.

Estimating LST from the in situ measurements has advantages, but there are two issues to discuss. First, there is the issue of site representativeness. There may be some inhomogeneous sites so that the 'point' measurements may not be able to represent the entire pixel. We initially selected the sites and the STD of the selected sites were below 3 K. Through experiments, we found that removing the selected sites with

larger STD (above 2 K) has basically no effect on the overall accuracy of the model, showing in the Table 5. The reason may be that the number of samples with the STD of site larger than 2 K is very small compared to total samples. When the sites were kept only with STD below 1 K, the accuracies were slightly improved by 0.208 K and 0.161 K for clear-sky model and cloudy-sky model, respectively. In addition, we further examined the relationship between the heterogeneity of selected sites and estimation accuracy shown in Fig. 13. There was no significant correlation between estimation accuracy and the site heterogeneity under both clear-sky conditions ($R = 0.336$) and cloudy-sky conditions ($R = 0.206$). This illustrated that the heterogeneities of the selected sites in this study had no significant impact on the model construction.

As initially clarified in Cao et al. (2019), the thermal radiation directionality (TRD) leads to the definition differences of MODIS LST and in situ LST extracted from pyrgeometer measurement. The in situ LST measurement (i.e., the reference of our RF LST product) is close to hemispherical LST, while MODIS LST is a directional LST. Since we used the in situ LST to construct the model, there may be differences between our product and MODIS LST. Thus, we made a further comparison. Fig. 14 shows the spatial distribution and corresponding histogram of the estimated LST bias against MODIS LST from 2010 to 2011. The bias statistics are mean = 0.80 K, STD = 1.28 K. The overall results are relatively consistent, but there are differences in the western CONUS. The differences probably come from the relatively high heterogeneity (Xu et al., 2019) and thermal radiation directionality (TRD) effect (Cao et al., 2019), which is more pronounced in complex terrains. Many studies have reported the large differences of LST under different view angles (Cao et al., 2021; Hu et al., 2016). MODIS LST is observed from

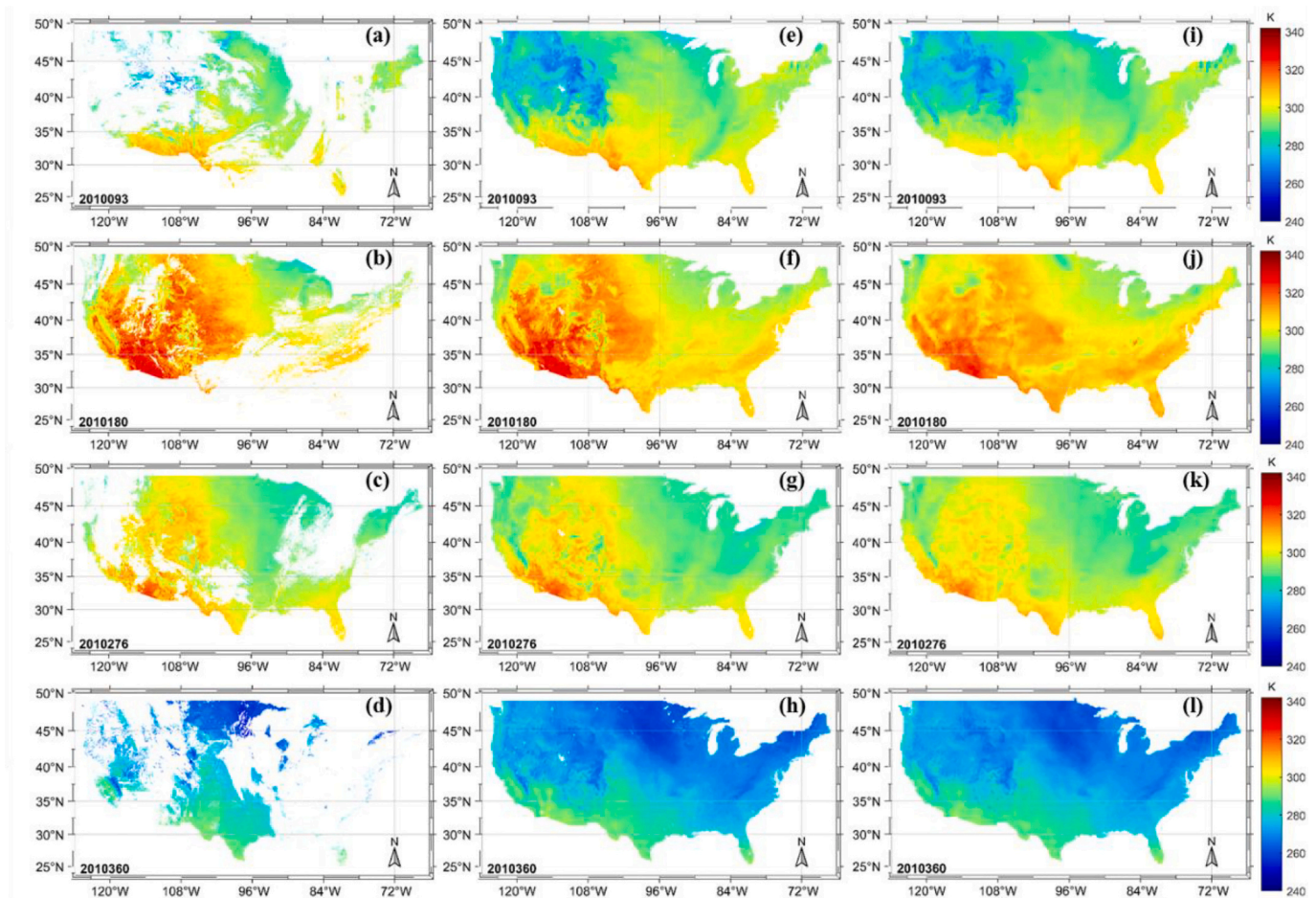


Fig. 10. (a-d) Original Terra MODIS LST daytime LST images, (d-h) estimated LST images, and (i-l) their corresponding GLDAS LST images on four different days in 2010 (93, 180, 276, 360 Julian days).

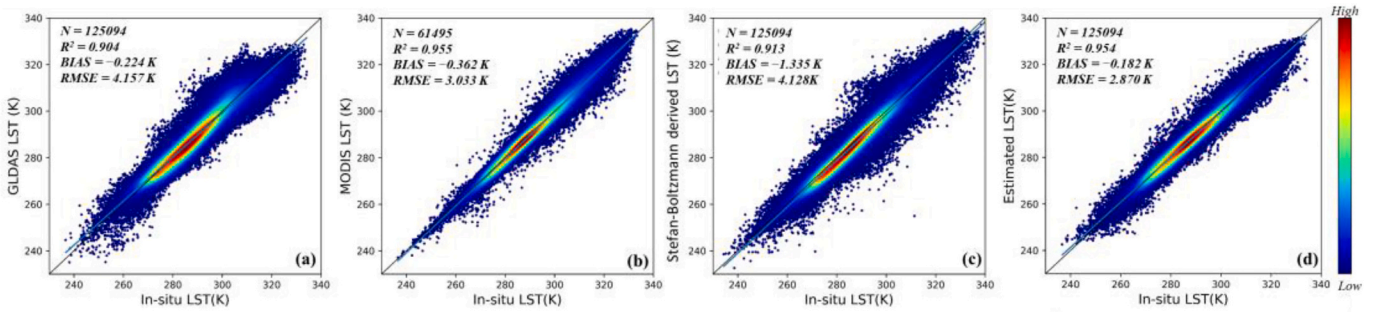


Fig. 11. Density scatterplots of (a) GLDAS LST, (b) clear-sky MODIS LST, (c) Stefan-Boltzmann derived LST and (d) estimated all-sky LST from independent validation dataset.

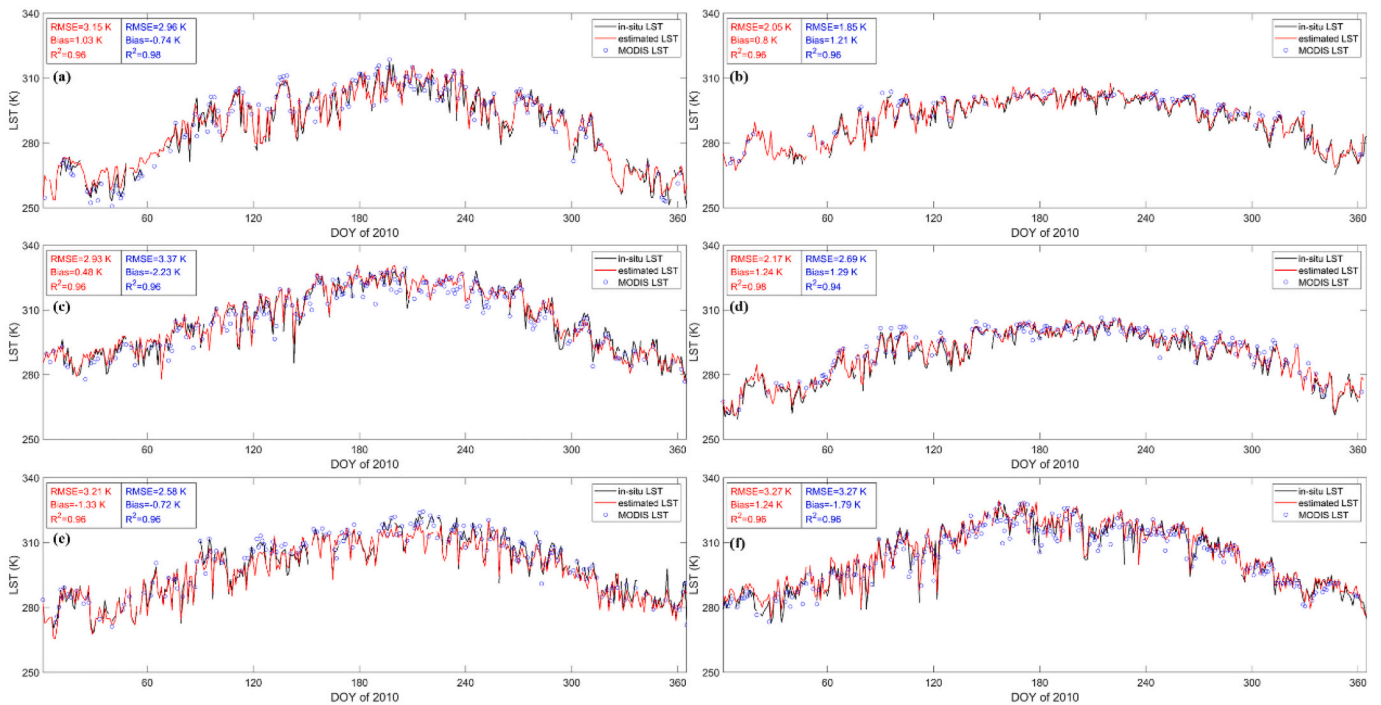


Fig. 12. Time series for in situ LST, estimated all-sky LST, and clear-sky MODIS LST in 2010 six sites at different regions. The latitude and longitude of the sites are: (a) 48.30783°, -105.1017°; (b) 35.93109°, -84.33242°; (c) 36.62373°, -116.01947°; (d) 38.7441°, -92.2°; (e) 36.6358°, -99.5975°; (f) -34.3349°, 106.7442°. The altitudes are 634, 381, 1004, 239, 647, and 1596 m, respectively. The statistical metrics of estimated LST and MODIS LST against in situ LST are displayed in red and blue, respectively. (For interpretation of the references to colour in this figure legend, the reader is referred to the web version of this article.)

Table 5

The accuracy of different independent datasets selected based on the STD value of sites.

Range of STD (K)	Clear sky		Cloudy sky	
	RMSE (K)	N	RMSE (K)	N
0-1	2.525	38,801	2.602	40,186
0-2	2.733	58,863	2.761	60,123
0-3	2.756	61,495	2.767	63,599

0° ups to >60°, while the proposed LST retrieval from in situ LST. The difference of view angles may lead to the difference between the estimated LST and MODIS LST. Meanwhile, we have compared the error distribution via the VZA of the estimated LST and MODIS LST, using the separated validation dataset. The error distribution is shown in Fig. 15. The error of the estimated LST is relatively stable with the change of VZA. However, as for MODIS LST, with the increase of VZA, the part where the density points gather gradually deviates from 0. TRD is a

complicated process and is not the research content of this study, therefore, we did not discuss it further. From the above comparison, difference exists between the estimated LST and MODIS LST. Theoretically and in practice, in contrast to MODIS LST, our proposed LST is less affected by the observation angle.

Compared with previous research, the method proposed in this paper has certain advantages. First, the variables used in this paper are all from optical remote sensing and reanalysis products, which are all-sky data and worldwide. Thus, it provides a possibility to expand the proposed method to other regions. In contrast to the PMW data, the data used avoided dealing with the uncertainty caused by different sampling depths and swath gaps. Meanwhile, the data used has a continuous and long sequence, which can be used to produce long-term continuous all-weather LST products. Second, the model is trained with real in situ LSTs instead of clear-sky MODIS LSTs for both clear-sky and cloudy-sky conditions, thus avoiding obtaining the hypothetic cloudy LST. Meanwhile, using the in situ LSTs reduced the uncertainty caused by different view angles. Third, with the development of advanced remote sensing data, the method proposed in this paper uses sufficient radiation

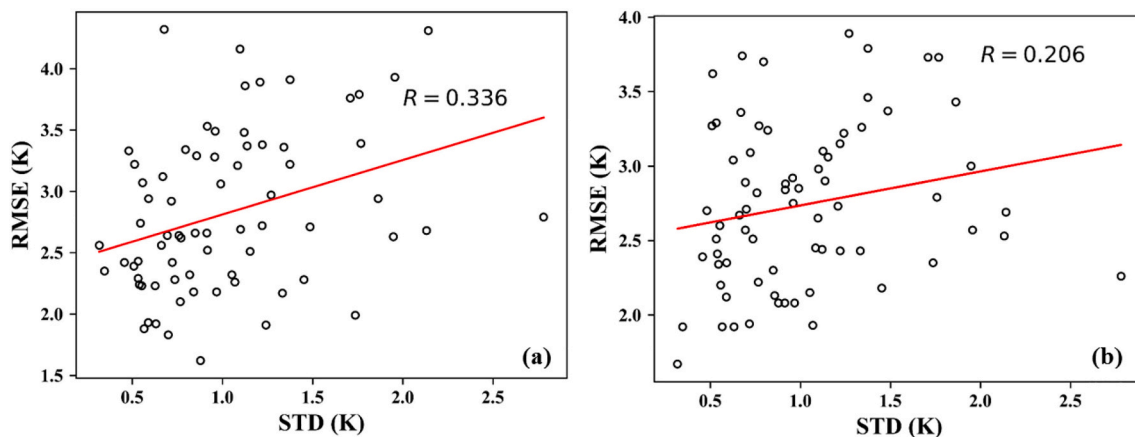


Fig. 13. The relationship between site accuracy and site STD under (a) clear-sky condition and (b) cloudy-sky condition.

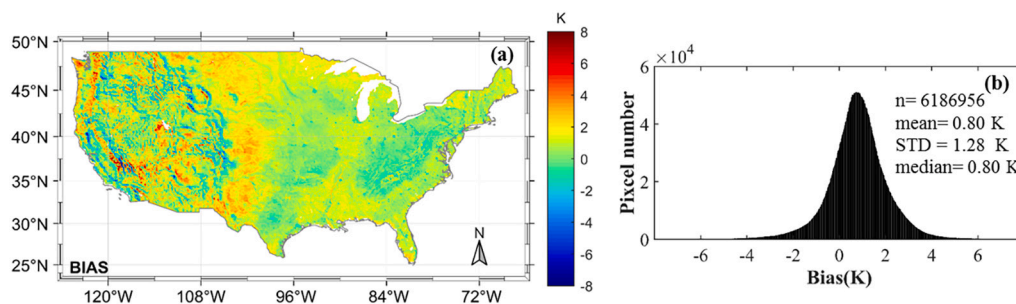


Fig. 14. Spatial patterns of statistical metrics of (a) bias between the estimated LST and MODIS LST under clear-sky conditions, and corresponding frequency distribution histograms (b) from 2010 to 2011.

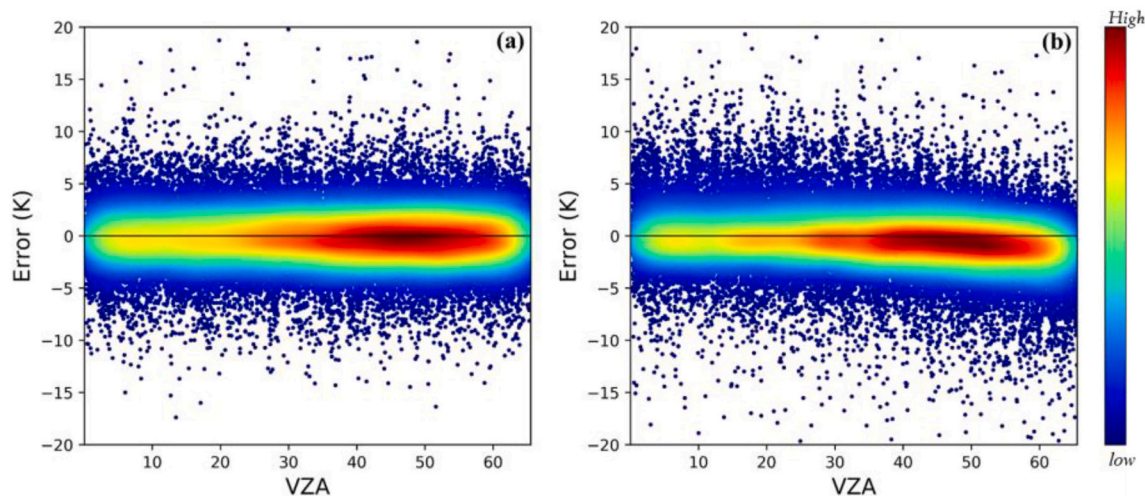


Fig. 15. The error distributions of the estimated LST (a) and MODIS LST (b) against in situ LST from the separated validation dataset.

variables including LDWN and DSR with high resolution, which considered the LST under the cloudy-sky condition, and was affected by changing the solar radiation and downward longwave radiation. Furthermore, the proposed method has high efficiency. Once the models are trained, they can be easily used for generating long time series all-sky LST products. The generated product can be used for agricultural drought monitoring, climate change analysis, and also as input to estimate other parameters, such as air temperature, soil moisture, etc.

However, the method also has limitations. Although the highest possible amount of representative ground stations in the long-term

sequence was selected and an independent dataset was used for validation, it was still difficult to quantitatively evaluate the areas without in situ observations. In addition, on the surface types of ice, snow, and barren, as well as areas with high thermal heterogeneity, the accuracy was relatively low, which is a difficulty also faced by other methods. In the future, the effects of surface terrain and spatial information should be considered, and deep learning should be incorporated to explore a more adaptive model using the information provided by remote sensing observations and data products, such as geostationary satellite sensors.

6. Conclusions

We aimed to estimate LST under all-sky conditions from different product data and other ancillary information. To achieve this, sufficient variables from optical remote sensing and reanalysis data were used, including radiation variables, land surface characteristic variables, and geographical and topographical parameters. All variables were available under all-sky conditions and contributed to the estimation of LST after feature optimization. To further improve the model performance under cloudy-sky conditions, temporal information was introduced in the RF model. This procedure was applied for instantaneous observations from both MOD and MYD sensors to obtain daily LST at daytime and nighttime. The major conclusions are shown as follows.

(1) For the cloudy-sky and clear-sky models, the validation results of the proposed models presented high accuracy, with RMSE = 2.767 and 2.756 K; $R^2 = 0.943$ and 0.963 ; bias = -0.143 and -0.138 K, respectively. The T-RF method used for the cloudy-sky model presented a slightly higher accuracy than the traditional RF method (RMSE = 2.914 K, bias = -0.191 K, $R^2 = 0.937$). There were no significant differences in the accuracy between clear-sky and cloudy-sky estimations. The 10-fold CV results (RMSE = 2.616 K, and 2.474 K) indicate that the constructed models have a robust performance.

(2) The accuracies of individual sites from the separated dataset are 1.67 K–3.89 K under cloudy-sky conditions. In contrast, those under clear-sky condition are 1.62 K–4.32 K, which is comparable to MODIS LST. The sites in the western part of CONUS have relatively lower accuracy, especially in mountainous areas. Besides, in contrast to MODIS LST, the estimated LST in this study is less affected by the directionality effect.

(3) In terms of temporal variability, the estimated LSTs were highly consistent with in situ LST and comparable with MODIS LST. The performance of the proposed method was excellent for daily LST estimation since daily LST variation and extreme events were captured. In terms of the spatial distribution, the estimated LSTs have the similar patterns with MODIS LST and effectively fill the data gaps. Besides, the estimated LSTs have more spatial details than GLDAS LST under all-sky conditions. The estimated LST (RMSE = 2.870 K) has higher accuracy than GLDAS LST (RMSE = 4.157 K), Stefan-Boltzmann derived LST (RMSE = 4.128 K) and MODIS LST (RMSE = 3.033 K).

Thermal infrared sensors are unable to provide LST data under cloudy-sky conditions. High-accuracy all-sky LSTs with 1 km resolution are in high demand. The proposed methodology is a feasible way to predict LST at high spatial and temporal resolution under all-sky conditions at all land cover types during daytime and nighttime. It provides a new framework and advances capabilities for reconstructing other sensors and other regions using local data. This capability will be beneficial for land surface monitoring and ecological dynamics. However, this method does not consider spatial information. Future development should focus on using deep learning methods that consider both temporal and spatial information.

Author contribution

Shunlin Liang and Bing Li designed the research and developed the methodology; Yan Chen and Tianchen Liang collected the data. Bing Li and Xiaobang Liu processed satellite images; Bing Li wrote the manuscript; Shunlin Liang, Han Ma and all other authors revised the manuscript.

Declaration of Competing Interest

The authors declare that they have no conflict.

Acknowledgements

This study was partially supported by the Chinese Grand Research

Program on Climate Change and Response under the project 2016YFA0600103. We gratefully acknowledge the data support from "National Earth System Science Data Center, National Science & Technology Infrastructure of China" (<http://www.geodata.cn>). The product will also be downloaded at www.glass.umd.edu. We also thank the National Aeronautics and Space Administration team for providing the MODIS products and GLDAS data freely download via the website <https://earthdata.nasa.gov/>. Additionally, authors would like to acknowledge the SURFRAD networks (<ftp://ftp.cmdl.noaa.gov/data/radiation/surfrad/>) and AmeriFlux networks (<https://ameriflux.lbl.gov/>) that provide available in situ measurements in this study.

References

- Augustine, J.A., DeLuisi, J.J., Long, C.N., 2000. SURFRAD—a national surface radiation budget network for atmospheric research. *Bull. Am. Meteorol. Soc.* 81, 2341–2357.
- Augustine, J.A., Hodges, G.B., Cornwall, C.R., Michalsky, J.J., Medina, C.I., 2005. An update on SURFRAD—the GCOS surface radiation budget network for the continental United States. *J. Atmos. Ocean. Technol.* 22, 1460–1472.
- Baldocchi, D., Falge, E., Gu, L., Olson, R., Hollinger, D., Running, S., Anthoni, P., Bernhofer, C., Davis, K., Evans, R., Fuentes, J., Goldstein, A., Katul, G., Law, B., Lee, X., Malhi, Y., Meyers, T., Munger, W., Oechel, W., Paw, K.T., Pilegaard, K., Schmid, H.P., Valentini, R., Verma, S., Vesala, T., Wilson, K., Wofsy, S., 2001. FLUXNET: a new tool to study the temporal and spatial variability of ecosystem-scale carbon dioxide, water vapor, and energy flux densities. *Bull. Am. Meteorol. Soc.* 82, 2415–2434.
- Belgiu, M., Drăguț, L., 2016. Random forest in remote sensing: a review of applications and future directions. *ISPRS J. Photogramm. Remote Sens.* 114, 24–31.
- Breiman, L., 2001. Random forests. *Mach. Learn.* 45, 5–32.
- Cao, B., Liu, Q., Du, Y., Roujean, J.-L., Gastellu-Etchegorry, J.-P., Trigo, I.F., Zhan, W., Yu, Y., Cheng, J., Jacob, F., Lagouarde, J.-P., Bian, Z., Li, H., Hu, T., Xiao, Q., 2019. A review of earth surface thermal radiation directionality observing and modeling: historical development, current status and perspectives. *Remote Sens. Environ.* 232.
- Cao, B., Roujean, J.-L., Gastellu-Etchegorry, J.-P., Liu, Q., Du, Y., Lagouarde, J.-P., Huang, H., Li, H., Bian, Z., Hu, T., Qin, B., Ran, X., Xiao, Q., 2021. A general framework of kernel-driven modeling in the thermal infrared domain. *Remote Sens. Environ.* 252, 112157.
- Cavaliere, D.J., Markus, T., Comiso, J.C., 2014. AMSR-E/Aqua Daily L3 25 km Brightness Temperature & Sea Ice Concentration Polar Grids, Version 3. [Indicate subset used]. NASA National Snow and Ice Data Center Distributed Active Archive Center. In, Boulder, Colorado USA.
- Cheng, J., Liang, S., Yao, Y., Ren, B., Shi, L., Liu, H., 2014. Comparative study of three land surface broadband emissivity datasets from satellite data. *Remote Sens.* 6, 111–134.
- Cheng, J., Liang, S., Verhoef, W., Shi, L., Liu, Q., 2016. Estimating the hemispherical broadband longwave emissivity of global vegetated surfaces using a radiative transfer model. *IEEE Trans. Geosci. Remote Sens.* 54 (2), 905–917.
- Cheng, J., Liang, S., Wang, W., Guo, Y., 2017. An efficient hybrid method for estimating clear-sky surface downward longwave radiation from MODIS data. *J. Geophys. Res.-Atmos.* 122, 2616–2630.
- Coll, C., Caselles, V., Galve, J., Valor, E., Niclos, R., Sanchez, J., Rivas, R., 2005. Ground measurements for the validation of land surface temperatures derived from AATSR and MODIS data. *Remote Sens. Environ.* 97, 288–300.
- Coops, N.C., Duro, D.C., Wulder, M.A., Han, T., 2007. Estimating afternoon MODIS land surface temperatures (LST) based on morning MODIS overpass, location and elevation information. *Int. J. Remote Sens.* 28, 2391–2396.
- Crosson, W.L., Al-Hamdan, M.Z., Hemmings, S.N.J., Wade, G.M., 2012. A daily merged MODIS aqua-Terra land surface temperature data set for the conterminous United States. *Remote Sens. Environ.* 119, 315–324.
- De Jeu, R.A., 2003. Retrieval of Land Surface Parameters Using Passive Microwave Remote Sensing. PhD diss., Vrije Universiteit Amsterdam.
- Duan, S.-B., Li, Z.-L., Leng, P., 2017. A framework for the retrieval of all-weather land surface temperature at a high spatial resolution from polar-orbiting thermal infrared and passive microwave data. *Remote Sens. Environ.* 195, 107–117.
- Duan, S.B., Li, Z.L., Wu, H., Leng, P., Gao, M.F., Wang, C.G., 2018. Radiance-based validation of land surface temperature products derived from collection 6 MODIS thermal infrared data. *Int. J. Appl. Earth Obs. Geoinf.* 70, 84–92.
- Duan, S.B., Li, Z.L., Li, H., Gottsche, F.M., Wu, H., Zhao, W., Leng, P., Zhang, X., Coll, C., 2019. Validation of collection 6 MODIS land surface temperature product using in situ measurements. *Remote Sens. Environ.* 225, 16–29.
- Ermida, S.L., Soares, P., Mantas, V., Göttsche, F.-M., Trigo, I.F., 2020. Google earth engine open-source code for land surface temperature estimation from the Landsat series. *Remote Sens.* 12, 1471.
- Gibson, R., Danaher, T., Hehir, W., Collins, L., 2020. A remote sensing approach to mapping fire severity in south-eastern Australia using sentinel 2 and random forest. *Remote Sens. Environ.* 240, 111702.
- Han, H., Guo, X., Yu, H., 2016. Variable Selection Using Mean Decrease Accuracy and Mean Decrease Gini Based on Random Forest, 219–224.
- Han, X.-J., Duan, S.-B., Huang, C., Li, Z.-L., 2018. Cloudy land surface temperature retrieval from three-channel microwave data. *Int. J. Remote Sens.* 40, 1793–1807.
- Hu, L., Monaghan, A., Voogt, J.A., Barlage, M., 2016. A first satellite-based observational assessment of urban thermal anisotropy. *Remote Sens. Environ.* 181, 111–121.

- Hutengs, C., Vohland, M., 2016. Downscaling land surface temperatures at regional scales with random forest regression. *Remote Sens. Environ.* 178, 127–141.
- Jackson, T.J., Chen, J.M., Gong, P., Liang, S., Yu, W., Wu, T., Nan, Z., Zhao, L., Wang, Z., 2014. A Novel Interpolation Method for MODIS Land Surface Temperature Data on the Tibetan Plateau, 9260, p. 92600Y.
- Jia, A., Ma, H., Liang, S., Wang, D., 2021. Cloudy-sky land surface temperature from VIIRS and MODIS satellite data using a surface energy balance-based method. *Remote Sens. Environ.* 263, 112566.
- Jiao, Z.-H., Yan, G., Wang, T., Mu, X., Zhao, J., 2019. Modeling of land surface thermal anisotropy based on directional and equivalent brightness temperatures over complex terrain. *IEEE J. Select. Top. Appl. Earth Observ. Remote Sens.* 12, 410–423.
- Jin, M., Dickinson, R.E., 2000. A generalized algorithm for retrieving cloudy sky skin temperature from satellite thermal infrared radiances. *J. Geophys. Res.-Atmos.* 105, 27037–27047.
- Kilibarda, M., Hengl, T., Heuvelink, G.B.M., Graeler, B., Pebesma, E., Tadic, M.P., Bajat, B., 2014. Spatio-temporal interpolation of daily temperatures for global land areas at 1 km resolution. *J. Geophys. Res.-Atmos.* 119, 2294–2313.
- Kuter, S., 2021. Completing the machine learning saga in fractional snow cover estimation from MODIS Terra reflectance data: random forests versus support vector regression. *Remote Sens. Environ.* 255, 112294.
- Lagouarde, J.P., Hénon, A., Irvine, M., Voogt, J., Pigeon, G., Moreau, P., Masson, V., Mestayer, P., 2012. Experimental characterization and modelling of the nighttime directional anisotropy of thermal infrared measurements over an urban area: case study of Toulouse (France). *Remote Sens. Environ.* 117, 19–33.
- Li, Z.-L., Tang, B.-H., Wu, H., Ren, H., Yan, G., Wan, Z., Trigo, I.F., Sobrino, J.A., 2013. Satellite-derived land surface temperature: current status and perspectives. *Remote Sens. Environ.* 131, 14–37.
- Li, H., Sun, D., Yu, Y., Wang, H., Liu, Y., Liu, Q., Du, Y., Wang, H., Cao, B., 2014. Evaluation of the VIIRS and MODIS LST products in an arid area of Northwest China. *Remote Sens. Environ.* 142, 111–121.
- Li, X., Zhou, Y., Asrar, G.R., Zhu, Z., 2018. Creating a seamless 1 km resolution daily land surface temperature dataset for urban and surrounding areas in the conterminous United States. *Remote Sens. Environ.* 206, 84–97.
- Liang, S., 2005. Quantitative Remote Sensing of Land Surfaces. John Wiley & Sons.
- Liang, S., Wang, J., 2019. Advanced Remote Sensing: Terrestrial Information Extraction and Applications. Academic Press.
- Liang, S., Cheng, J., Jia, K., Jiang, B., Liu, Q., Xiao, Z., Yao, Y., Yuan, W., Zhang, X., Zhao, X., 2020. The global LAnd surface satellite (GLASS) product suite. *Bull. Am. Meteorol. Soc.* 1–37.
- Liaw, A., Wiener, M., 2002. Classification and regression by randomForest. *R News* 2, 18–22.
- Liu, N.F., Liu, Q., Wang, L.Z., Liang, S.L., Wen, J.G., Qu, Y., Liu, S.H., 2013. A statistics-based temporal filter algorithm to map spatiotemporally continuous shortwave albedo from MODIS data. *Hydrol. Earth Syst. Sci.* 17, 2121–2129.
- Long, D., Yan, L., Bai, L., Zhang, C., Li, X., Lei, H., Yang, H., Tian, F., Zeng, C., Meng, X., Shi, C., 2020. Generation of MODIS-like land surface temperatures under all-weather conditions based on a data fusion approach. *Remote Sens. Environ.* 246.
- Louppe, G., Wehenkel, L., Sutura, A., Geurts, P., 2013. Understanding variable importances in forests of randomized trees. *Adv. Neural Inf. Process. Syst.* 431–439.
- Ma, H., Liang, S., Xiao, Z., Shi, H., 2017. Simultaneous inversion of multiple land surface parameters from MODIS optical-thermal observations. *ISPRS J. Photogramm. Remote Sens.* 128, 240–254.
- Ma, H., Liang, S., Xiao, Z., Wang, D., 2018. Simultaneous estimation of multiple land-surface parameters from VIIRS optical-thermal data. *IEEE Geosci. Remote Sens. Lett.* 15, 156–160.
- Metz, M., Rocchini, D., Neteler, M., 2014. Surface temperatures at the continental scale: tracking changes with remote sensing at unprecedented detail. *Remote Sens.* 6, 3822–3840.
- Metz, M., Andreo, V., Neteler, M., 2017. A new fully gap-free time series of land surface temperature from MODIS LST data. *Remote Sens.* 9, 1333.
- Neteler, M., 2010. Estimating daily land surface temperatures in mountainous environments by reconstructed MODIS LST data. *Remote Sens.* 2, 333–351.
- Padhee, S.K., Dutta, S., 2020. Spatiotemporal reconstruction of MODIS land surface temperature with the help of GLDAS product using kernel-based nonparametric data assimilation. *J. Appl. Remote. Sens.* 14, 014520.
- Pede, T., Mountrakis, G., 2018. An empirical comparison of interpolation methods for MODIS 8-day land surface temperature composites across the conterminous United States. *ISPRS J. Photogramm. Remote Sens.* 142, 137–150.
- Pedregosa, F., Varoquaux, G., Gramfort, A., Michel, V., Thirion, B., Grisel, O., Blondel, M., Prettenhofer, P., Weiss, R., Dubourg, V., 2011. Scikit-learn: machine learning in Python. *J. Mach. Learn. Res.* 12, 2825–2830.
- Pelletier, C., Valero, S., Inglada, J., Champoin, N., Dedieu, G., 2016. Assessing the robustness of random forests to map land cover with high resolution satellite image time series over large areas. *Remote Sens. Environ.* 187, 156–168.
- Prigent, C., Rossow, W.B., Matthews, E., Marticorena, B., 1999. Microwave radiometric signatures of different surface types in deserts. *J. Geophys. Res.-Atmos.* 104, 12147–12158.
- Qu, Y., Liu, Q., Liang, S., Wang, L., Liu, N., Liu, S., 2014. Direct-estimation algorithm for mapping daily land-surface broadband Albedo from MODIS data. *IEEE Trans. Geosci. Remote Sens.* 52, 907–919.
- Rodell, M., Houser, P.R., Jambor, U., Gottschalck, J., Mitchell, K., Meng, C.J., Arsenault, K., Cosgrove, B., Radakovich, J., Bosilovich, M., Entin, J.K., Walker, J.P., Lohmann, D., Toll, D., 2004. The global land data assimilation system. *Bull. Am. Meteorol. Soc.* 85, 381–394.
- Shen, H., Li, X., Cheng, Q., Zeng, C., Yang, G., Li, H., Zhang, L., 2015. Missing information reconstruction of remote sensing data: a technical review. *Ieee Geosci. Remote Sens. Magaz.* 3, 61–85.
- Shwetha, H.R., Kumar, D.N., 2016. Prediction of high spatio-temporal resolution land surface temperature under cloudy conditions using microwave vegetation index and ANN. *ISPRS J. Photogramm. Remote Sens.* 117, 40–55.
- Urquhart, E.A., Hoffman, M.J., Murphy, R.R., Zaitchik, B.F., 2013. Geospatial interpolation of MODIS-derived salinity and temperature in the Chesapeake Bay. *Remote Sens. Environ.* 135, 167–177.
- Wan, Z., Dozier, J., 1996. A generalized split-window algorithm for retrieving land-surface temperature from space. *IEEE Trans. Geosci. Remote Sens.* 34, 892–905.
- Wan, Z., Li, Z.-L., 1997. A physics-based algorithm for retrieving land-surface emissivity and temperature from EOS/MODIS data. *IEEE Trans. Geosci. Remote Sens.* 35, 980–996.
- Wan, Z., Zhang, Y., Zhang, Q., Li, Z.-L., 2002. Validation of the land-surface temperature products retrieved from Terra moderate resolution imaging Spectroradiometer data. *Remote Sens. Environ.* 83, 163–180.
- Wang, K., Liang, S., 2009. Evaluation of ASTER and MODIS land surface temperature and emissivity products using long-term surface longwave radiation observations at SURFRAD sites. *Remote Sens. Environ.* 113, 1556–1565.
- Wang, W., Liang, S., Meyers, T., 2008. Validating MODIS land surface temperature products using long-term nighttime ground measurements. *Remote Sens. Environ.* 112, 623–635.
- Wang, T., Shi, J., Ma, Y., Husi, L., Comyn-Platt, E., Ji, D., Zhao, T., Xiong, C., 2019. Recovering land surface temperature under cloudy skies considering the solar-cloud-satellite geometry: application to MODIS and Landsat-8 data. *J. Geophys. Res.-Atmos.* 124, 3401–3416.
- Wei, J., Huang, W., Li, Z., Xue, W., Peng, Y., Sun, L., Cribb, M., 2019. Estimating 1-km-resolution PM_{2.5} concentrations across China using the space-time random forest approach. *Remote Sens. Environ.* 231, 111221.
- Wei, J., Li, Z., Cribb, M., Huang, W., Xue, W., Sun, L., Guo, J., Peng, Y., Li, J., Lyapustin, A., Liu, L., Wu, H., Song, Y., 2020. Improved 1 km resolution PM_{2.5} estimates across China using enhanced space-time extremely randomized trees. *Atmos. Chem. Phys.* 20, 3273–3289.
- Williamson, S.N., Hik, D.S., Gamon, J.A., Jarosch, A.H., Anslow, F.S., Clarke, G.K., Rupp, T.S., 2017. Spring and summer monthly MODIS LST is inherently biased compared to air temperature in snow covered sub-Arctic mountains. *Remote Sens. Environ.* 189, 14–24.
- Wu, P., Yin, Z., Yang, H., Wu, Y., Ma, X., 2019. Reconstructing geostationary satellite land surface temperature imagery based on a multiscale feature connected convolutional neural network. *Remote Sens.* 11, 300.
- Xiao, Z., Liang, S., Wang, J., Chen, P., Yin, X., Zhang, L., Song, J., 2014. Use of general regression neural networks for generating the GLASS leaf area index product from time-series MODIS surface reflectance. *IEEE Trans. Geosci. Remote Sens.* 52, 209–223.
- Xiao, Z., Liang, S., Wang, J., Xiang, Y., Zhao, X., Song, J., 2016. Long-time-series global land surface satellite leaf area index product derived from MODIS and AVHRR surface reflectance. *IEEE Trans. Geosci. Remote Sens.* 54, 5301–5318.
- Xu, S., Cheng, J., Zhang, Q., 2019. Reconstructing all-weather land surface temperature using the Bayesian maximum entropy method over the Tibetan plateau and Heihe River basin. *IEEE J. Select. Top. Appl. Earth Observ. Remote Sens.* 12, 3307–3316.
- Yang, F., Cheng, J., 2020. A framework for estimating cloudy sky surface downward longwave radiation from the derived active and passive cloud property parameters. *Remote Sens. Environ.* 248, 111972.
- Yoo, C., Im, J., Cho, D., Yokoya, N., Xia, J., Bechtel, B., 2020. Estimation of all-weather 1 km MODIS land surface temperature for humid summer days. *Remote Sens.* 12.
- Yu, Y., Privette, J.L., Pinheiro, A.C., 2005. Analysis of the NPOESS VIIRS land surface temperature algorithm using MODIS data. *IEEE Trans. Geosci. Remote Sens.* 43, 2340–2350.
- Yu, W., Ma, M., Wang, X., Tan, J., 2014. Estimating the land-surface temperature of pixels covered by clouds in MODIS products. *J. Appl. Remote. Sens.* 8, 083525.
- Zeng, C., Shen, H., Zhong, M., Zhang, L., Wu, P., 2015. Reconstructing MODIS LST based on multitemporal classification and robust regression. *IEEE Geosci. Remote Sens. Lett.* 12, 512–516.
- Zeng, C., Long, D., Shen, H., Wu, P., Cui, Y., Hong, Y., 2018. A two-step framework for reconstructing remotely sensed land surface temperatures contaminated by cloud. *ISPRS J. Photogramm. Remote Sens.* 141, 30–45.
- Zhan, W., Chen, Y., Zhou, J., Wang, J., Liu, W., Voogt, J., Zhu, X., Quan, J., Li, J., 2013. Disaggregation of remotely sensed land surface temperature: literature survey, taxonomy, issues, and caveats. *Remote Sens. Environ.* 131, 119–139.
- Zhang, X., Pang, J., Li, L., 2015. Estimation of land surface temperature under cloudy skies using combined diurnal solar radiation and surface temperature evolution. *Remote Sens.* 7, 905–921.
- Zhang, Q., Yuan, Q., Zeng, C., Li, X., Wei, Y., 2018. Missing data reconstruction in remote sensing image with a unified spatial-temporal-spectral deep convolutional neural network. *IEEE Trans. Geosci. Remote Sens.* 56, 4274–4288.
- Zhang, S., Duan, S.-B., Li, Z.-L., Huang, C., Wu, H., Han, X.-J., Leng, P., Gao, M., 2019a. Improvement of Split-window algorithm for land surface temperature retrieval from sentinel-3A SLSTR data over barren surfaces using ASTER GED product. *Remote Sens.* 11, 3025.
- Zhang, X., Wang, D., Liu, Q., Yao, Y., Jia, K., He, T., Jiang, B., Wei, Y., Ma, H., Zhao, X., 2019b. An operational approach for generating the global land surface downward shortwave radiation product from MODIS data. *IEEE Trans. Geosci. Remote Sens.* 57, 4636–4650.
- Zhang, X., Zhou, J., Gottsche, F.-M., Zhan, W., Liu, S., Cao, R., 2019c. A method based on temporal component decomposition for estimating 1-km all-weather land surface

- temperature by merging satellite thermal infrared and passive microwave observations. *IEEE Trans. Geosci. Remote Sens.* 57, 4670–4691.
- Zhang, X., Zhou, J., Liang, S., Chai, L., Wang, D., Liu, J., 2020. Estimation of 1-km all-weather remotely sensed land surface temperature based on reconstructed spatial-seamless satellite passive microwave brightness temperature and thermal infrared data. *ISPRS J. Photogramm. Remote Sens.* 167, 321–344.
- Zhang, X., Zhou, J., Liang, S., Wang, D., 2021. A practical reanalysis data and thermal infrared remote sensing data merging (RTM) method for reconstruction of a 1-km all-weather land surface temperature. *Remote Sens. Environ.* 260, 112437.
- Zhao, W., Duan, S.-B., 2020. Reconstruction of daytime land surface temperatures under cloud-covered conditions using integrated MODIS/Terra land products and MSG geostationary satellite data. *Remote Sens. Environ.* 247.
- Zhao, W., Duan, S.-B., Li, A., Yin, G., 2019. A practical method for reducing terrain effect on land surface temperature using random forest regression. *Remote Sens. Environ.* 221, 635–649.
- Zhao, B., Mao, K., Cai, Y., Shi, J., Li, Z., Qin, Z., Meng, X., Shen, X., Guo, Z., 2020. A combined Terra and Aqua MODIS land surface temperature and meteorological station data product for China from 2003 to 2017. *Earth Syst. Sci. Data* 12, 2555–2577.
- Zhou, J., Dai, F., Zhang, X., Zhao, S., Li, M., 2015. Developing a temporally land cover-based look-up table (TL-LUT) method for estimating land surface temperature based on AMSR-E data over the Chinese landmass. *Int. J. Appl. Earth Obs. Geoinf.* 34, 35–50.